Arabian Journal for Science and Engineering (2022) 47:7309–7323
https://doi.org/10.1007/s13369-021-06232-z

RESEARCH ARTICLE-EARTH SCIENCES

3-D Rock-Physics Templates for the Seismic Prediction of Pore Microstructure in Ultra-Deep Carbonate Reservoirs

Uti I. Markus[1,3] · Jing Ba[1] · José M. Carcione[1,2] · Lin Zhang[1] · Mengqiang Pang[1]

Received: 22 June 2021 / Accepted: 13 September 2021 / Published online: 10 October 2021

Abstract

Ultra-deep carbonate reservoirs have low porosity, a complex pore space with microcracks of varying aspect ratio and dissolved pores, that affect the seismic and transport properties. We propose a rock-physics model based on penny-shaped inclusions in the framework of the double-porosity theory to estimate rock features, such as the crack porosity and aspect ratio, and stiff porosity. Based on this model, a 3-D rock-physics template is built, calibrated at the ultrasonic and seismic frequency bands, from attenuation, P-wave impedance and V_P/V_S ratio to quantitatively evaluate the effect of those features. Attenuation is estimated by using the spectral-ratio and improved frequency-shift methods. The template is applied to ultra-deep carbonates of the S work area of the Tarim Basin (China). The predictions agree with the well-log data and field production reports. In general, the higher the crack aspect ratio, the higher the storage and transport capacity of the reservoir. Therefore, these crack features can be used as indicators of these reservoir properties.

Keywords Penny-shaped inclusion · Double-porosity theory · Crack aspect ratio · Crack porosity · 3-D rock-physics template · Ultra-deep carbonate reservoirs

1 Introduction

With the depletion of conventional reservoirs and the improvement of oil exploration methods, ultra-deep carbonates such as those in the Tarim basin and Sichuan basin started to be investigated [1]. Multi-phase structural development and composite diagenetic history, resulting in various reservoir heterogeneities, characterize these Chinese basins [2]. The textural and mineral composition of carbonate rocks are affected by complex diagenesis, which leads to the generation of a complex pore [3]. As a result, the primary porosity tends to diminish, enhancing the secondary porosity caused by mineral dissolution during deep burial conditions [4, 5] and generating microcracks, broad fractures, moldic and vuggy pores, and caverns [6].

Low porosity, small pore-throat diameter, complex pore space, clay content, and low permeability are features of tight rocks [7–10]. The pore structure is an important factor that affects the seismic and transport properties [11–20]. Aspect ratio is another critical factor [21, 22]. Rocks with a high aspect ratio (vuggy and moldic pores) are stiff and affect less the seismic waves, whereas rocks with a low aspect ratio (cracks) have a more pronounced effect [23–25]. Kumar and Han [26] developed a model to evaluate aspect ratio and density in carbonate rocks from brine saturated P-wave velocities, while Sayers [27] examined the relations between pore aspect ratio and elastic properties. Smith [28] studied the effect of pore aspect ratio on the velocities and resistivity of tight-gas sand, with compliant (soft) porosity playing an important role. Zhao et al. [29] used well-logs and seismic data to propose a model that describes the pore-type distribution of carbonates quantitatively.

Rock-physics templates (RPTs) establish a relationship between the elastic attributes such as density, velocity, and acoustic impedance, and the reservoir characteristic such as porosity, lithology, fluid saturation, and permeability [30–32]. The relationship between acoustic impedance (AI)

✉ Jing Ba
jba@hhu.edu.cn

1 School of Earth Sciences and Engineering, Hohai University, Nanjing 211100, China

2 Istituto Nazionale Di Oceanografia E Di Geofisica Sperimentale (OGS), Borgo Grotta Gigante 42c, 34010 Sgonico, Trieste, Italy

3 Department of Soil Science and Land Resources Management, Federal University Wukari, Wukari P.M.B 1020, Nigeria

and the phase-velocity ratio is often used in RPTs for fluid and lithology identification [30, 33]. Li and Zhang [34] built a 3-D RPT to characterize the composite pore system of carbonates from seismic data and well-logs. Tan et al. [35] used ultrasonic data and effective-medium theory to build a rock-physics template for the seismic prediction of tight-siltstone reservoir brittleness, and Pang et al. [36] applied multiscale RPTs to estimate the crack porosity of deep carbonate reservoirs.

This study establishes a model for the seismic prediction of crack aspect ratio. The model employs the self-consistent approximation (SCA) [37] in addition to the penny-shaped inclusion theory [38] to build 3-D multiscale RPTs for deep carbonate reservoirs. The templates are calibrated with ultrasonic and seismic data to evaluate also the total and microcrack porosities and their distribution in the subsurface.

2 Work Area and Target Formations

The *S* area belongs to the zone of Shuntuoguole uplift, which is located within the Northcentral of Tarim Basin, one of the hydrocarbon accumulation basins of northwest China with an area coverage of about 560,000 km^2 [39, 40]. The target formations are the Yijianfang and Yingshan formations (Ordovician) deposited and formed during the Caledonian-Hercynian orogeny [41]. The reservoirs are characterized by microcracks, dissolved pores, karst caves, and vugs formed by multi-phase structural developments and complex diagenesis. An average thickness of 110 m characterizes the reservoir, temperatures higher than 150 °C, and confining pressures more than 160 MPa.

3 Model and Data

3.1 Conceptual Model and Thin Carbonate Section

The schematic representation in Fig. 1a shows a host medium comprising spherical pores and cracks with varying aspect ratios assumed to be penny-shaped inclusions randomly oriented and distributed. The cracks are assumed to be penny-shaped inclusions because they tend to capture some essential properties such as the pressure dependency of elastic properties characterized by preferential closure of compliant pores that gives an idealization of real cracks. The penny-shaped microcrack inclusion is considered to have a radius R_o and height h, with a crack aspect ratio of $\alpha = h/2R_o$, as shown in Fig. 1b. Figure 1c shows a thin slice of the carbonate sample, whose mineral constituents are calcite, dolomite, and clay, having a composition of 92%, 6%, and 2%, respectively. The slice shows dissolved pores and microcracks with varying aspect ratios and a very low surface porosity.

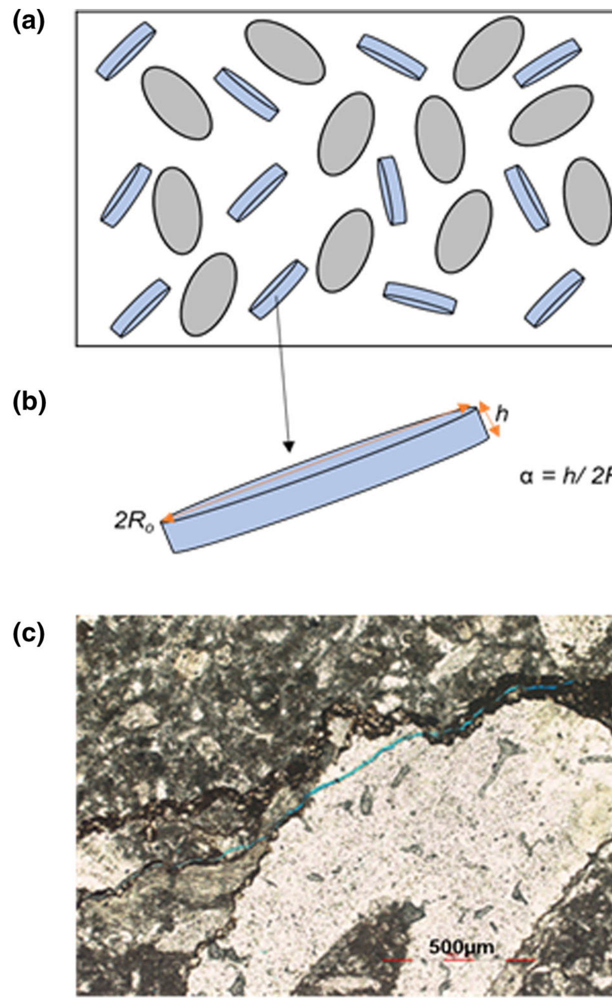

Fig. 1 **a** Schematic representation of the spherical pores and penny-shape microcracks, **b** Penny-shaped crack with the aspect ratio, **c** Rock sample thin section showing microcracks with varying apertures

3.2 Experimental Analysis

3.2.1 Estimation of Crack Properties

Two carbonates (limestone) samples A and B from the S area are used for ultrasonic wave experiments at 1 MHz. The samples are cylindrical with an average diameter of 25.2 mm. The reference material (aluminum block) with the same shape as each sample is prepared. The measured porosities, permeabilities, and dry-rock densities of samples A and B are 2.5% and 0.71%, 0.023 mD and 1.559 mD, and 2.66 g/cm^3 and 2.67 g/cm^3, respectively. Guo et al. [42] setup is adopted for the experiment and wave velocity is estimated at a temperature and pore pressure of 140 °C and 10 MPa, respectively.

The setup for the experiments consists of a digital oscilloscope and a pulse generator. The samples are saturated with oil using the vacuum and pressure method and then kept in a rubber jacket. We vary the confining pressure in the range 15–80 MPa with steps of 5 MPa. The first arrivals of the waveforms are picked to obtain the velocities.

The inversion method [20, 43] is used to compute the crack porosity from the confining and pore pressures, and P- and S-wave velocities.

We assume stiff and compliant (cracks) pores. First, we compute the bulk and shear moduli of the rock without cracks by adopting the Mori–Tanaka theory [44]:

$$K_{\text{stiff}} = \frac{K_s}{\left(1 + \frac{\phi_{\text{stiff}}}{1-\phi_{\text{stiff}}} P_s(\alpha_{\text{stiff}}, \upsilon_s)\right)}, \tag{1}$$

$$G_{\text{stiff}} = \frac{\mu_s}{\left(1 + \frac{\phi_{\text{stiff}}}{1-\phi_{\text{stiff}}} Q_s(\alpha_{\text{stiff}}, \upsilon_s)\right)}, \tag{2}$$

where ϕ_{stiff} is the stiff porosity, K_s and μ_s are the bulk and shear moduli of grain, respectively, α_{stiff} is the stiff pore aspect ratio, υ_s is the Poisson ratio and P_s and Q_s are the normalized compressibility and shear compliances of the dry pores (see Appendix A). At high differential pressure, when the cracks are closed, the stiff pore aspect ratio α_{stiff} can be computed by a least-square algorithm applied to the elastic moduli.

Then, we apply the Mori–Tanaka theory neglecting the interaction between pores and cracks to obtain the effective dry-rock bulk and shear moduli (K_{eff} and G_{eff}) with randomly oriented penny-shaped cracks, which are compared with the experimental data to determine the crack properties.

$$K_{\text{eff}} = \frac{K_{\text{stiff}}}{\left(1 + \frac{16(1-(\upsilon_{\text{stiff}})^2)\Gamma}{9(1-2\upsilon_{\text{stiff}})}\right)}, \tag{3}$$

$$G_{\text{eff}} = \frac{G_{\text{stiff}}}{\left(1 + \frac{32(1-\upsilon_{\text{stiff}})(5-\upsilon_{\text{stiff}})\Gamma}{45(2-\upsilon_{\text{stiff}})}\right)}, \tag{4}$$

where Γ is the crack density and $\upsilon_{\text{stiff}} = (3K_{\text{stiff}} - 2G_{\text{stiff}})/(6K_{\text{stiff}}+2G_{\text{stiff}})$ is the Poisson ratio of the host material.

The aspect ratio is related to the differential pressure by [20]:

$$\alpha = \frac{4\left[1 - (\upsilon_{\text{eff}})^2\right] P_d}{\pi E_{\text{eff}}}, \tag{5}$$

where α is the crack aspect ratio, P_d is the differential pressure, $\upsilon_{\text{eff}} = (3K_{\text{eff}} - 2G_{\text{eff}})/(6K_{\text{eff}} + 2G)$ is the effective Poisson ratio and $E_{\text{eff}} = 3K_{\text{eff}}[1 - 2\upsilon_{\text{eff}}]$ is the effective Young modulus.

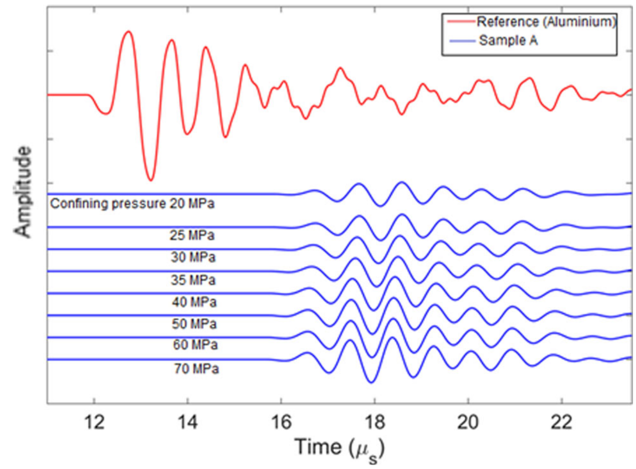

Fig. 2 Waveforms in the reference material and sample A

The crack porosity (ϕ_c) is related to the crack density by [43]:

$$\phi_c = \frac{4\pi\alpha}{3}\Gamma \tag{6}$$

3.2.2 Estimation of Ultrasonic Attenuation

The spectral-ratio method determines the quality factor Q by adopting a high quality factor medium as a reference [9, 45]. The equation is

$$\ln\left[\frac{A_1(f)}{A_2(f)}\right] = -\frac{\pi x}{QV} f + \ln\left[\frac{G_1(f)}{G_2(f)}\right], \tag{7}$$

where V is the sample wave velocity, x is the wave propagation distance, f is the frequency, $A_1(f)$ and $A_2(f)$, and $G_1(f)$ and $G_2(f)$ are the amplitude spectra and geometric factors of the sample and reference material, respectively.

3.3 Experimental Data

The waveforms in the reference medium and sample A are shown in Fig. 2, and Fig. 3 shows the results. Crack porosity decreases with increasing confining pressure, and P-wave velocity decreases with increasing crack porosity while V_P/V_S increases. The P-wave attenuation increases as the crack porosity increases.

4 Workflow the Procedure

4.1 Mineral Mixture

We assume that the carbonate is a mixture of two skeletons, which contain intergranular pores and cracks. The dominant mineral composition is calcite, with a small quantity of

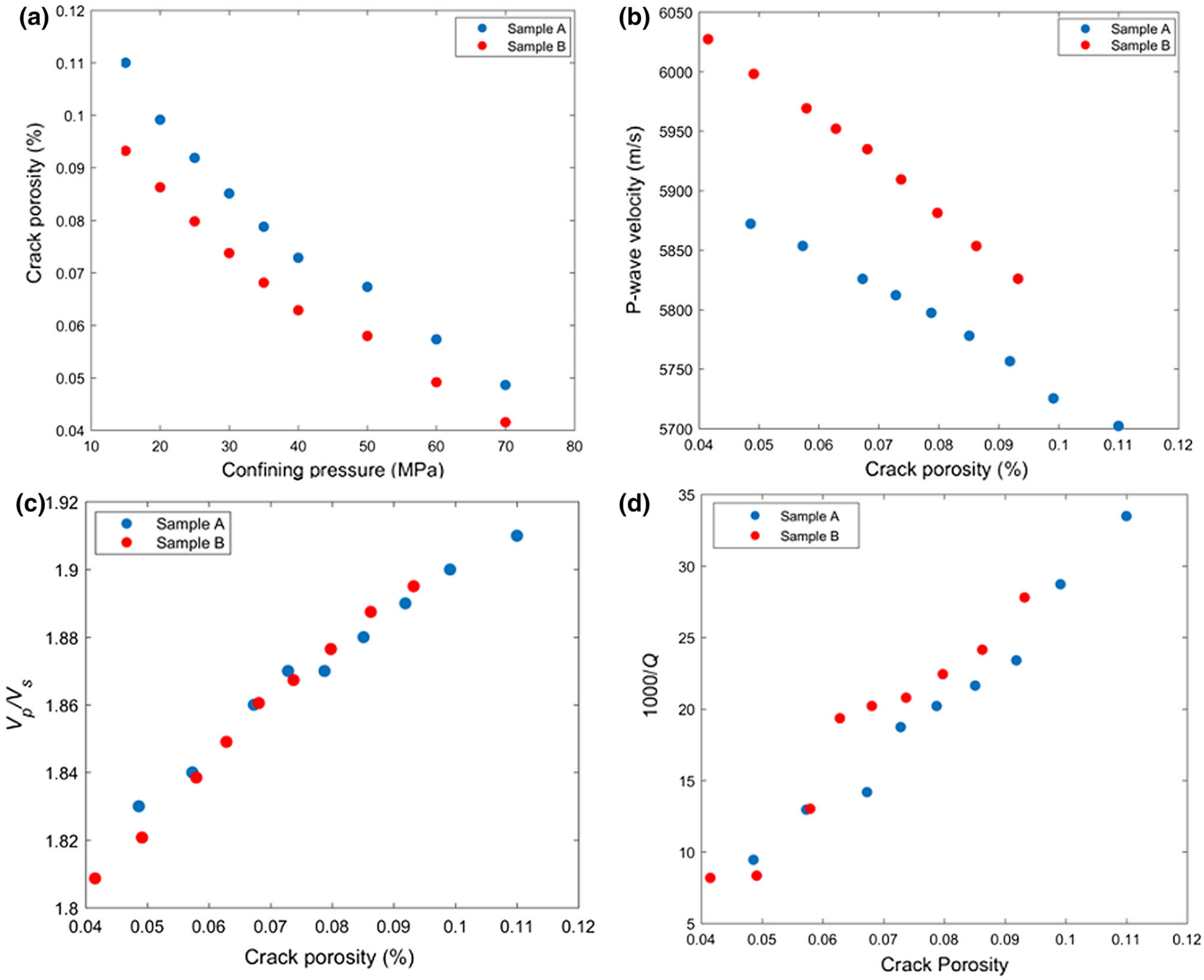

Fig. 3 Crack porosity and its relation with confining pressure (**a**), P-wave velocity (**b**), velocity ratio (V_P/V_S) (**c**), and P-wave dissipation factor (**d**)

dolomite and clay, having the following bulk and shear moduli (in GPa): 64.5 and 32.5, 74.5 and 47.5, and 23.2 and 11, respectively. The Voigt–Reuss–Hill (VRH) average [46–48] is utilized to estimate the moduli of the mineral mixture:

$$M_V = \sum_{i=1}^{N} f_i M_i, \tag{8a}$$

$$1/M_R = \sum_{i=1}^{N} f_i/M_i, \tag{8b}$$

$$M_{\mathrm{VRH}} = \frac{M_V + M_R}{2}, \tag{8c}$$

where i, f_i and M_i correspond to the mineral type, volume fraction, and elastic modulus, respectively, while M_V, M_R and M_{VRH} are the Voigt, Reuss, and Hill averages, respectively.

4.2 Dry-Rock Properties

According to the complexity and heterogeneity of the fabric, we assume the inter-granular pores (stiff pores) and cracks (soft pores) are spherical and penny-shaped, respectively. The stiff pore aspect ratio is set to 1, and values within the range of 10^{-5}–10^{-2} [42] are considered for the soft pores. The composite system of pores is assumed to be isotropic and interconnected (see Fig. 4).

In the rock physics modeling of this study, as is shown in Fig. 4, the SCA equation [49] is used to mix the pores and penny-shaped cracks to compute the dry-rock elastic moduli,

$$\sum x_i (K_i - K_{\mathrm{SC}}^*) P^{*i} = 0, \tag{9a}$$

$$\sum x_i (\mu_i - \mu_{\mathrm{SC}}^*) Q^{*i} = 0, \tag{9b}$$

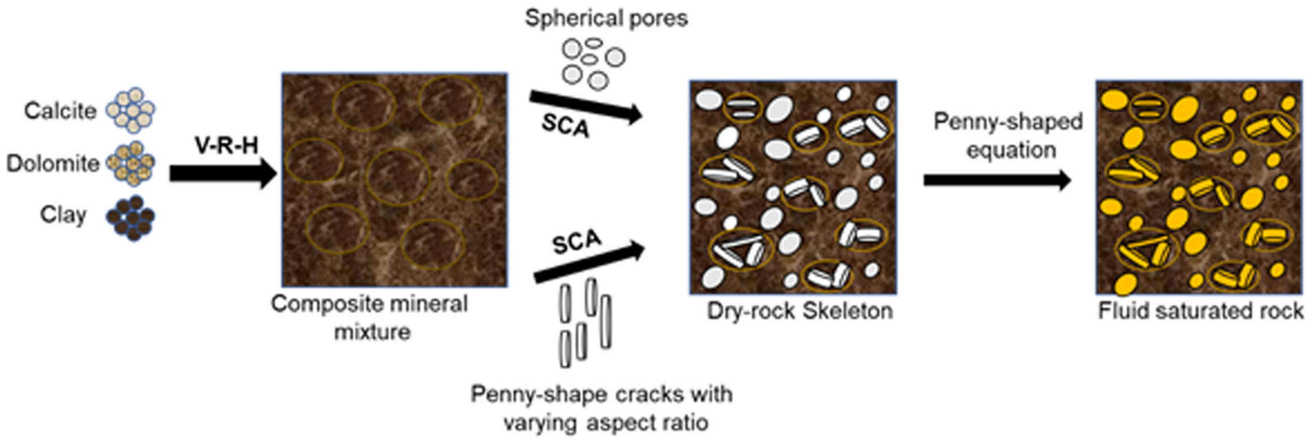

Fig. 4 Workflow of the methodology

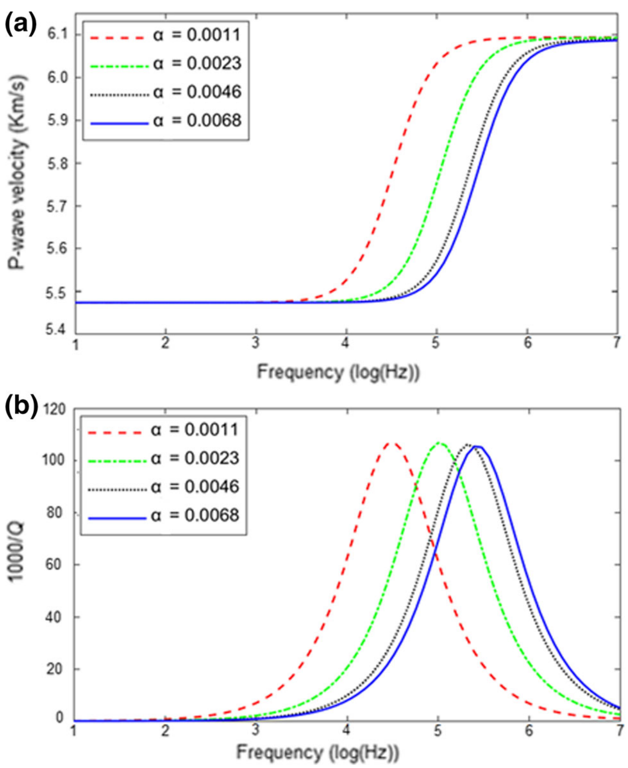

Fig. 5 P-wave velocity (**a**) and dissipation factor (**b**) as a function of frequency for different soft-pore aspect ratios

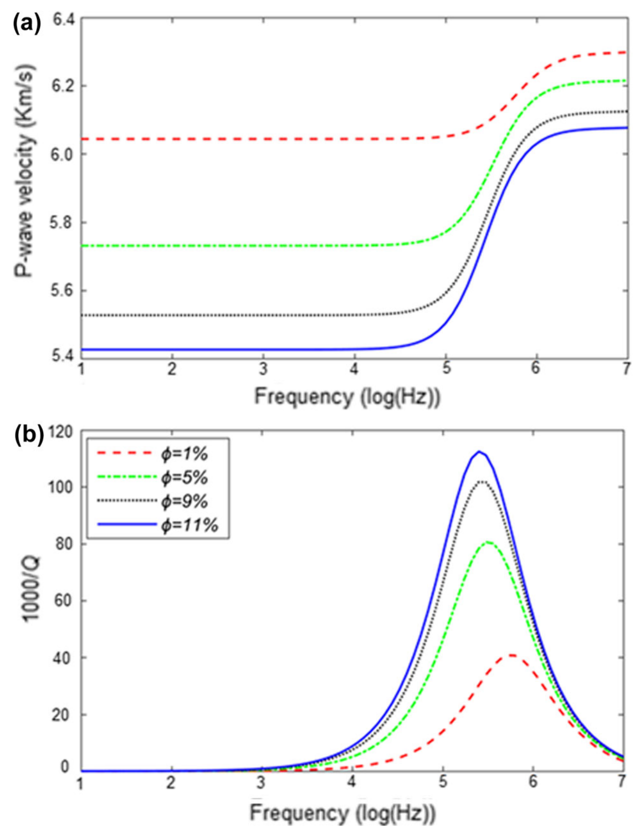

Fig. 6 P-wave velocity (**a**) and dissipation factor (**b**) as a function of frequency for different stiff porosities

where x_i, K_i and μ_i are the mineral phase volume fraction, bulk modulus, and shear modulus, respectively, K^*_{SC} and μ^*_{SC} are the bulk and shear moduli of dry rock, respectively, P^{*i} and Q^{*i} are the inclusion shape factors of the i phase (see Appendix B).

4.3 Fluid Substitution

Batzle and Wang [50] equations are used to estimate the fluid bulk modulus and density at in situ conditions. The Biot–Rayleigh theory describes the fluid flow between the pores and penny-shaped inclusions caused by the periodic oscillations of the waves [38, 51]. The penny-shaped inclusion model [38] is used for fluid substitution to obtain the saturated rock's wave properties. The local fluid flow mechanism between the host and penny-shaped inclusions, induced by the periodic oscillations of waves, generates the wave dissipation. The relevant differential equations,

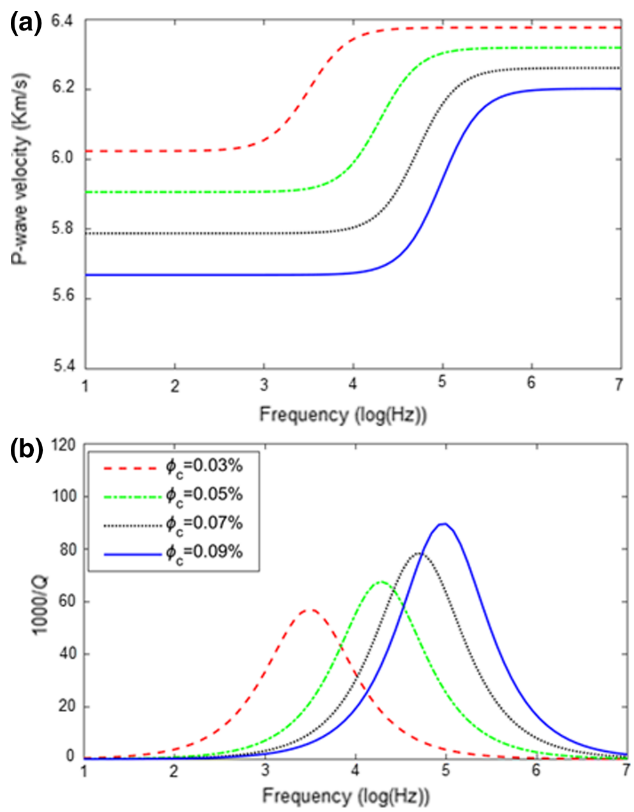

Fig. 7 P-wave velocity (**a**) and dissipation factor (**b**) as a function of frequency for different soft porosities

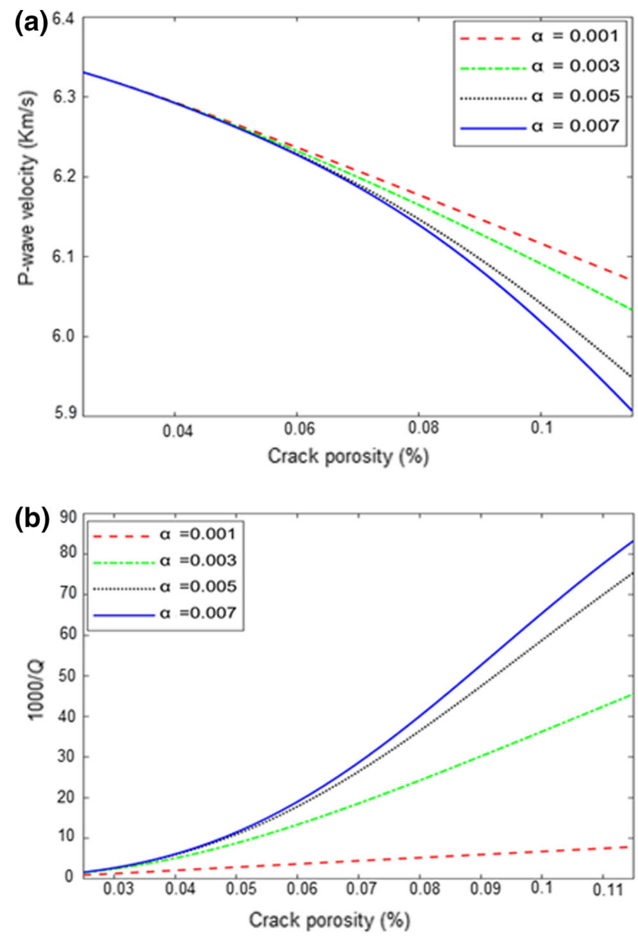

Fig. 8 P-wave velocity (**a**) and dissipation factor (**b**) as a function of crack porosity for different crack aspect ratios at 1 MHz

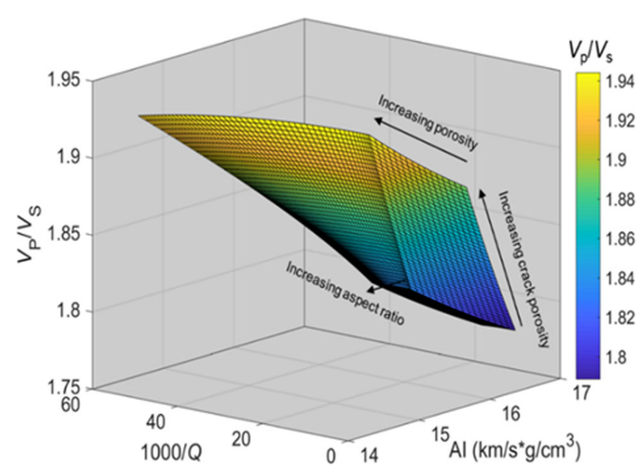

Fig. 9. 3-D Rock-Physics template at 1 MHz

stiffness coefficients, and dispersion equations are given in Appendices B, C, and D.

4.4 Wave Properties

The mineral components include calcite, dolomite, and clay, with a composition of 92%, 6%, and 2%, respectively. The inclusion radius is set based on the carbonate sample thin section, and the inclusion porosity ranges within 0.005–0.1. The inclusion can be modeled as a cylinder containing a transverse crack with an average effective aperture of several microns [36, 52, 53]. Thus, based on [36], the radius and porosity of the inclusion are set as 50 µm and 0.01, respectively. The oil bulk modulus, density, and viscosity are 1.789 GPa, 0.698 g/cm^3, and 0.00239 Pa s, respectively. The VRH average moduli and SCA equations are adopted to compute the mineral mixture and rock frame properties, and we analyze the relation between crack aspect ratio, total and crack porosities, and P-wave properties by assuming full oil saturation.

Figures 5, 6, and 7 show the P-wave velocity and attenuation for different crack aspect ratios, porosity, and crack porosity. In Fig. 5, the host and crack porosities are, respectively, 10% and 0.02%. The crack porosity and aspect ratio are fixed at 0.02% and 0.0034, respectively, and the total porosity varies, as indicated in Fig. 6. In Fig. 7, the total porosity and aspect ratio are 10% and 0.0034, respectively. It can be seen that the higher the crack aspect ratio, the relaxation peak moves to the high frequencies, while the peak

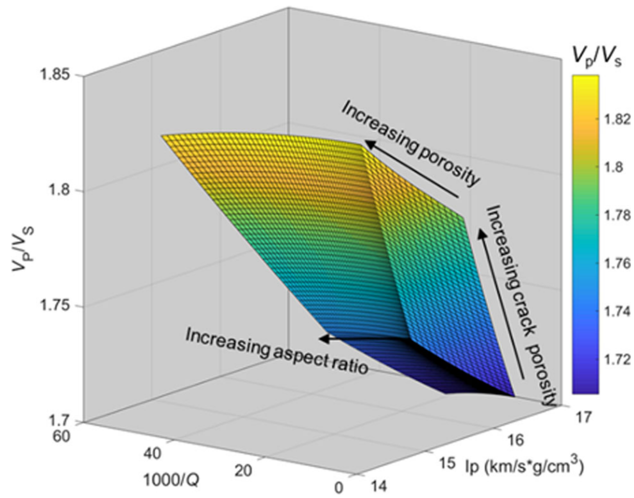

Fig. 10. 3-D Rock-Physics template at 35 Hz

dissipation factor remains constant, but attenuation increases with frequency (see Eq. 2.123 in [54]) with a slight increase in the relaxation frequency as the crack aspect ratio increases. Moreover, the higher the total or crack porosity, the higher the peak dissipation factor and the higher the P-wave dispersion. Figure 8a, b shows stronger attenuation and higher dispersion with a higher crack aspect ratio.

5 3-D Rock-Physics Template

A quantitative interpretation of reservoir log and seismic data can be achieved with rock-physics templates [55, 56]. Indeed, the relation between seismic properties and crack aspect ratio, and total and crack porosities can be used to build 3-D RPTs based on P-wave attenuation, impedance, and P/S velocity ratio. Such templates at 1 MHz and 35 Hz are shown in Figs. 9 and 10, respectively, where the color bar denotes V_P/V_S. With an inclusion radius of 50 mm, we have the attenuation peak at the seismic frequency band.

5.1 Calibration of the Template at Ultrasonic Frequencies

The 3-D RPT is calibrated at 1 MHz using two of the samples, whose data are scatters in Figs. 11 and 12. The black, blue, and red curves indicate constant crack aspect ratio, total porosity, and crack porosity, respectively. Figures 11 and 12 show the same trend, e.g., with an increasing porosity, the V_P/V_S ratio and attenuation increase and P-wave impedance decreases. Also, with an increasing crack aspect ratio, the V_P/V_S ratio and attenuation increase, and P-wave impedance decreases, while the attenuation and V_P/V_S ratio increase with crack porosity. As indicated by the color bar, the crack aspect ratio and crack porosity data points agree with the template.

5.2 Estimation of Seismic Attenuation

The sensitivity of seismic attenuation to hydrocarbon accumulation and fluid saturation in fracture systems has been acknowledged as a helpful tool for reservoir characterizations [57, 58]. To estimate the seismic reservoir attenuation, we adopt the improved frequency-shift method [59], with an assumption of a Ricker wavelet to calculate the quality factor,

$$Q = \frac{\sqrt{\pi^5} t f_{c1} f_{c0}^2}{16(f_{c0}^2 - f_{c1}^2)}, \tag{10}$$

Fig. 11 The 3-D RPT at 1 MHz data. The color bar gives the crack aspect ratio

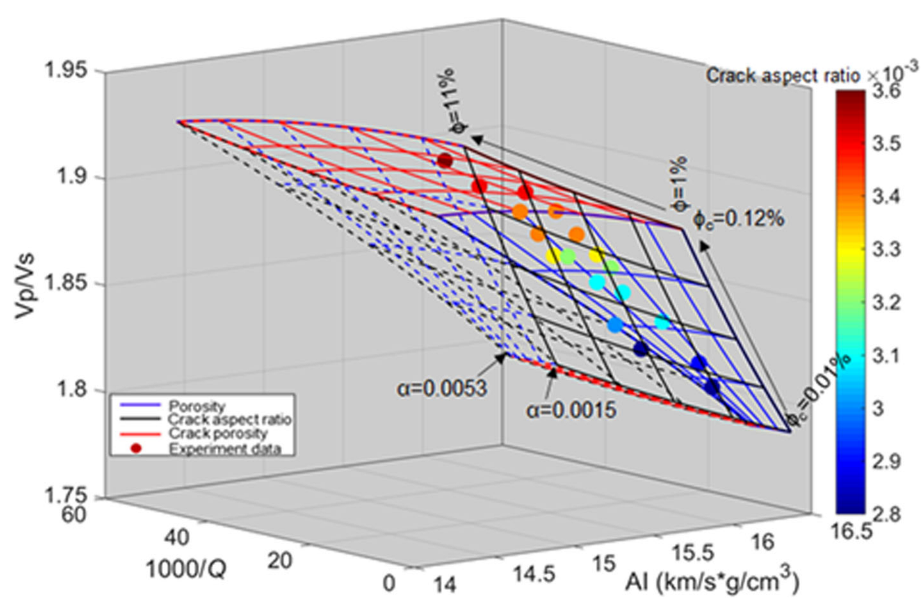

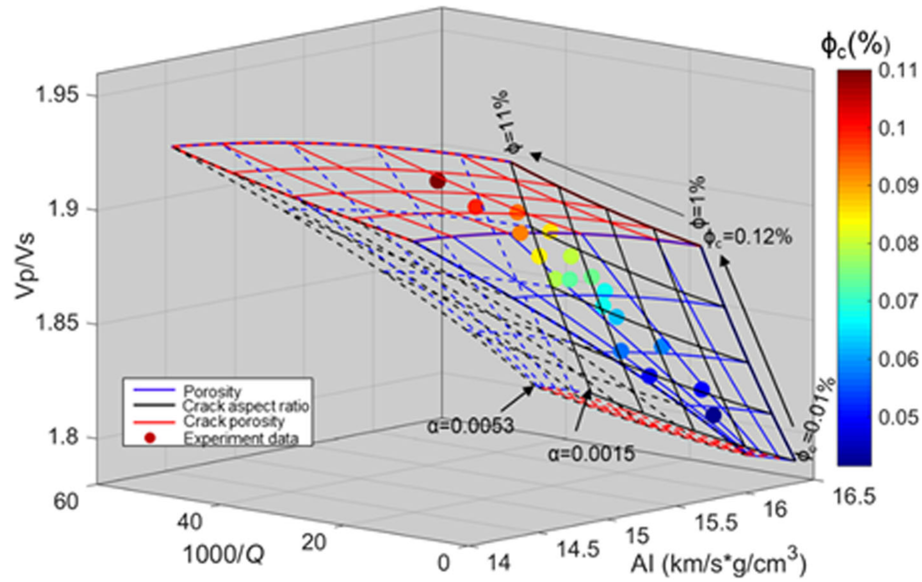

Fig. 12. 3-D RPT at 1 MHz data. The color bar gives the crack porosity

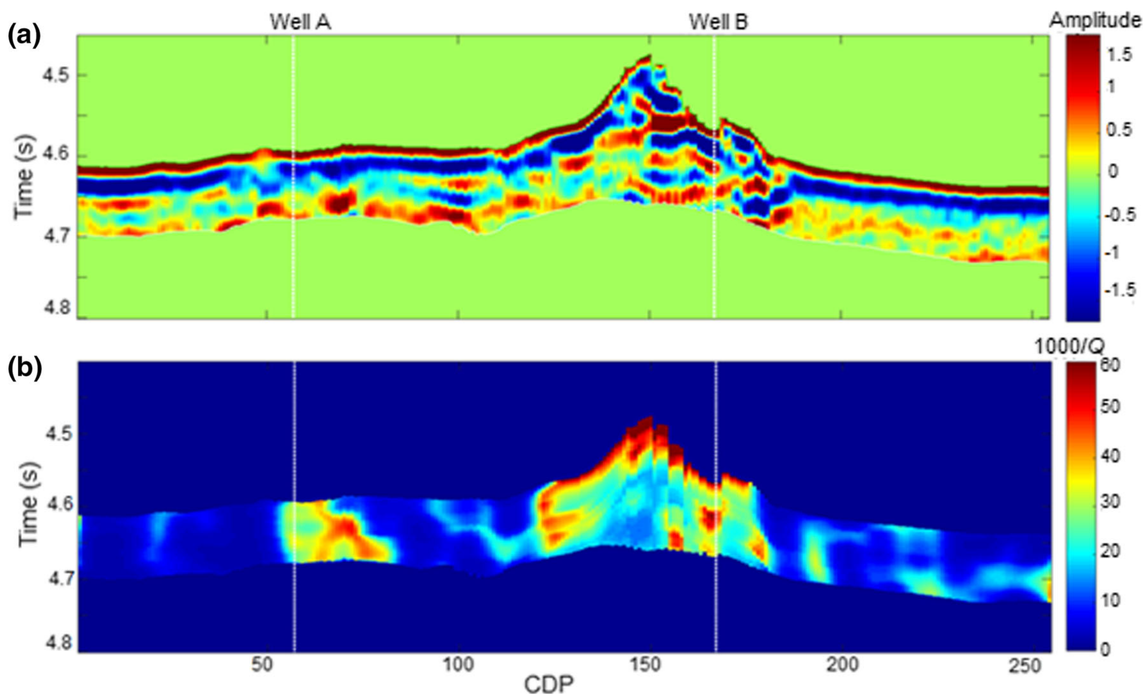

Fig. 13 2-D Seismic profiles. **a** Amplitude and **b** Dissipation factor

where t, f_{c0}, and f_{c1}, respectively, correspond to travel time, centroid frequency of the signal before wave propagation, and centroid frequency of the signal after wave propagation.

The target formation seismic amplitude and dissipation factor are, respectively, given in Fig. 13a, b, where the location of two wells is indicated. The red and blue colors, respectively, indicate strong and weak attenuation regions.

5.3 Calibration of the Template at the Seismic Band

Figures 14 and 15 show seismic properties and calibration at 35 Hz, respectively, where V_P/V_S and P-wave impedance are derived from 3-D pre-stack inversion and the log porosity is extracted from Well B. It shows that the seismic data agrees with the template (Fig. 15), with the color bar corresponding to porosity. The data indicates a low reservoir porosity that corresponds to the target-formation geological properties.

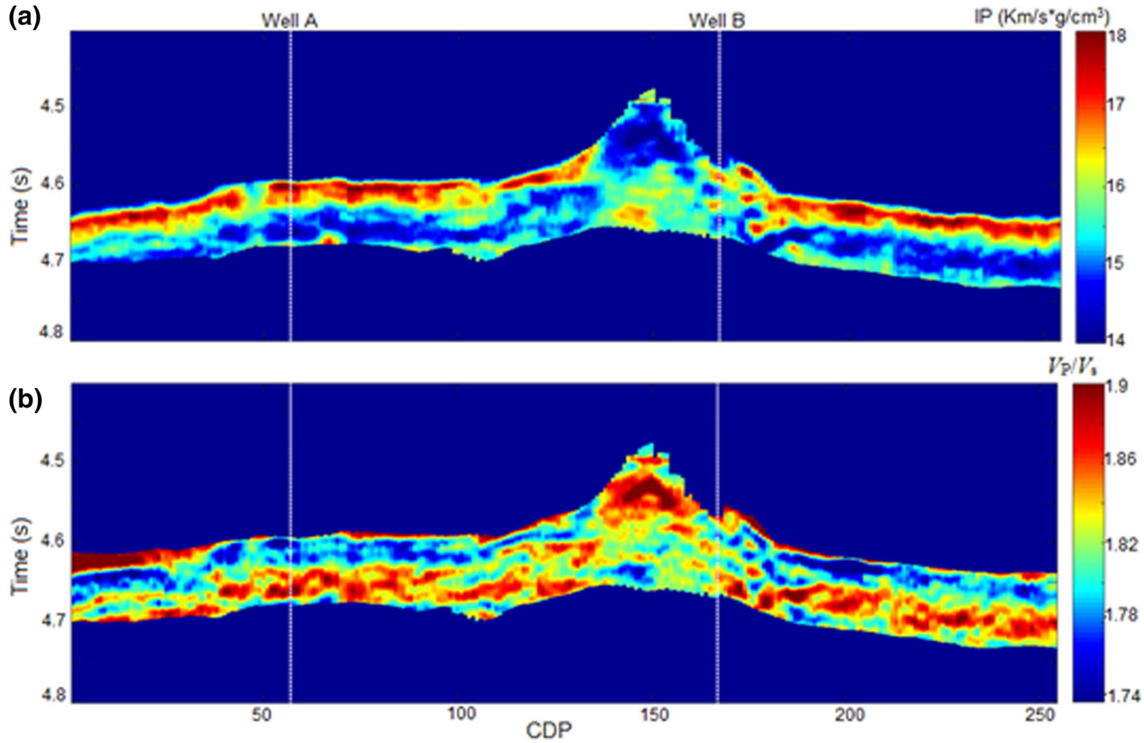

Fig. 14 Inversion results of a 2-D seismic line crossing Wells A and B. **a** P-wave impedance and **b** V_P/V_S

Fig. 15 The 3-D RPT at 35 Hz and field seismic data

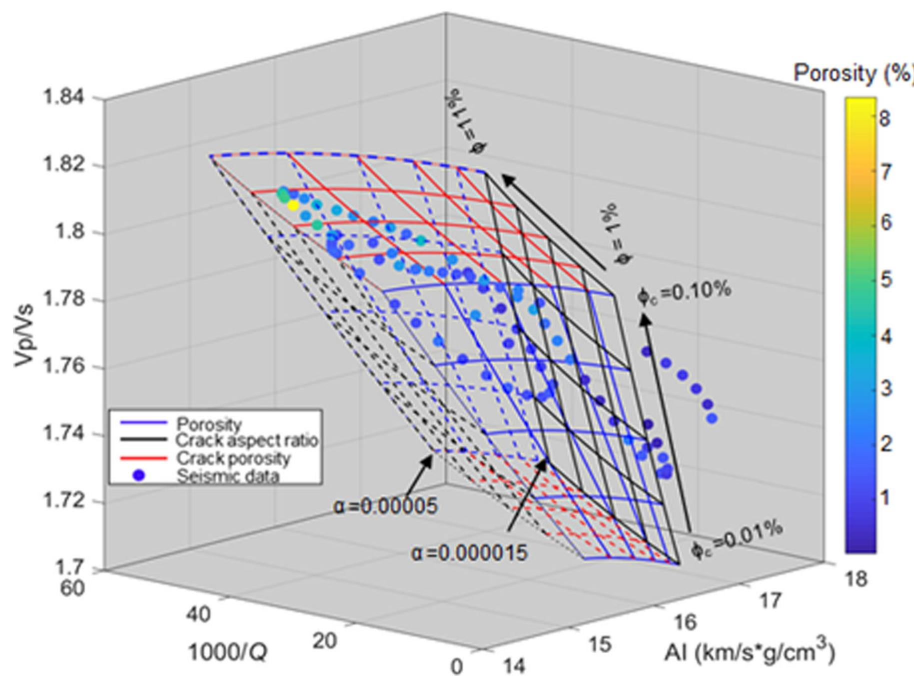

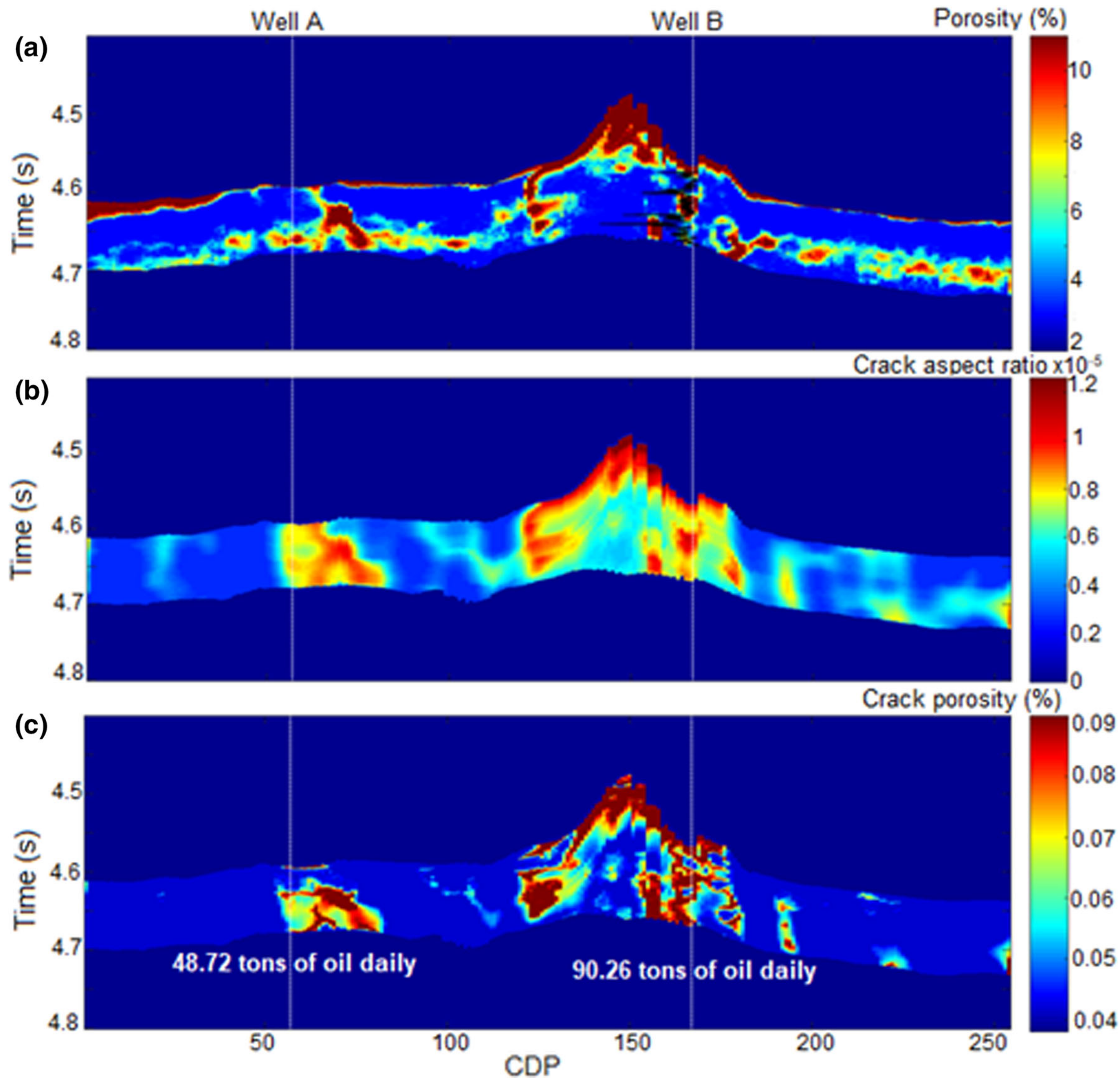

Fig. 16 Total porosity (**a**), crack aspect ratio (**b**), and crack porosity (**c**) on a 2-D profile crossing Wells A and B

6 Estimation of Reservoir Porosity, and Crack Aspect Ratio and Porosity

The rock properties are estimated around Wells A and B by overlaying the P-wave impedance, V_P/V_S, and dissipation factor on the template, where porosity, crack aspect ratio, and crack porosity correspond to the ranges 2–11%, 0.000003–0.000012, and 0.01–0.09%, respectively. Figure 16a indicates that a great part of the target formation has low porosity, suggesting tight rocks, and a higher porosity, crack aspect ratio and crack porosity in Well B than Well A (Fig. 16a–c).

A 3-D horizontal section of the crack aspect ratio, total porosity, and crack porosity is shown in Fig. 17. Well B shows a higher porosity, crack aspect ratio and crack porosity than Well A. The results agree with the actual production reports, which reveal a production capacity of 48.72 tons at well A and 90.26 tons at well B. Therefore, the results validate the predictions of the model.

7 Conclusions

We predict the pore microstructure of carbonate rocks from a poroelasticity model and rock-physics templates calibrated at ultrasonic and seismic frequencies. Basically, the methodology yields the crack (soft) porosity and aspect ratio, and the total (stiff) porosity. We use the self-consistent approximation to obtain the properties of the rock skeleton and the Biot–Rayleigh poroelasticity theory, based on penny-shaped inclusions to calculate the seismic rock properties (phase velocity and dissipation factor). P-wave impedance, V_P/V_S

Fig. 17 3-D horizontal section showing porosity (**a**), crack aspect ratio (**b**), and crack porosity (**c**)

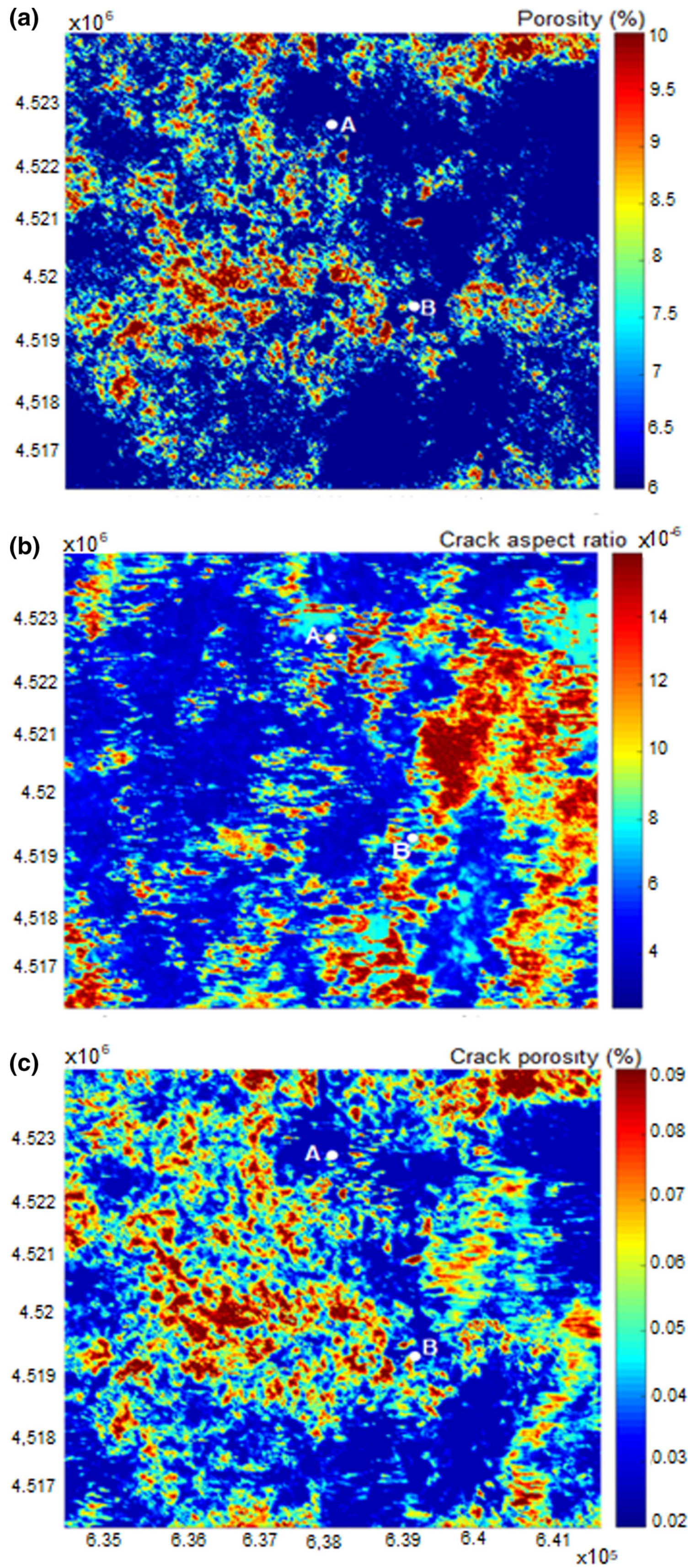

and attenuation are used to build 3-D rock-physics templates. The results agree with the production reports, showing that the methodology can be used to predict the characteristics of deep and ultra-deep carbonate reservoirs.

Acknowledgements The authors are grateful for the support of the National Natural Science Foundation of China (grant no. 41974123), the Jiangsu Innovation and Entrepreneurship Plan, and the Jiangsu Province Science Fund for Distinguished Young Scholars.

Appendix A: Factors *P* and *Q*

Following [20, 43], we have

$$P_s = \frac{(1-v_s)}{6(1-2v_s)} \times \frac{4(1+v_s) + 2\alpha_{\text{stiff}}^2(7-2v_s) - \left[3(1+4v_s) + 12\alpha_{\text{stiff}}^2(2-v_s)\right]g}{2\alpha_{\text{stiff}}^2 + (1-4\alpha_{\text{stiff}}^2)g + (\alpha_{\text{stiff}}^2 - 1)(1+v_s)g^2}, \tag{A1}$$

$$Q_s = \frac{4(\alpha_{\text{stiff}}^2 - 1)(1-v_s)}{15\left\{9(v_s-1) + 2\alpha_{\text{stiff}}^2(3-4v_s) + \left[(7-8v_s) - 4\alpha_{stiff}^2(1-2v_s)\right]g\right\}} \times \left\{ \begin{array}{l} \dfrac{8(1-v_s) + 2\alpha_{\text{stiff}}^2(3+4v_s) + \left[(8v_s-1) - 4\alpha^2(5+2v_s)\right]g + 6(\alpha_{\text{stiff}}^2-1)(1+v_s)g^2}{2\alpha_{\text{stiff}}^2 + (1-4\alpha_{\text{stiff}}^2)g + (\alpha_{\text{stiff}}^2-1)(1+v_s)g^2} \\ -3\left[\dfrac{8(v_s-1) + 2\alpha_{\text{stiff}}^2(5-4v_s) + \left[3(1-2v_s) + 6\alpha_{\text{stiff}}^2(v_s-1)\right]g}{-2\alpha_{\text{stiff}}^2 + \left[(2-v_s) + \alpha_{\text{stiff}}^2(1+v_s)\right]g}\right] \end{array} \right\} \tag{A2}$$

where

$$g = \begin{cases} \dfrac{\alpha_{\text{stiff}}^2}{(1-\alpha_{\text{stiff}}^2)^{3/2}}\left(\arccos \alpha_{\text{stiff}}^2 - \alpha_{\text{stiff}}^2\sqrt{1-\alpha_{\text{stiff}}^2}\right) & (\alpha_{\text{stiff}}^2 < 1) \\ \dfrac{\alpha_{\text{stiff}}^2}{(1-\alpha_{\text{stiff}}^2)^{3/2}}\left(\alpha_{\text{stiff}}^2\sqrt{1-\alpha_{\text{stiff}}^2} - \operatorname{arccos} h\, \alpha_{\text{stiff}}^2\right) & (\alpha_{\text{stiff}}^2 > 1) \end{cases} \tag{A3}$$

where $v_s = (3K_s - 2\mu_s)/(6K_s + 2\mu_s)$ is the Poisson ratio.

Appendix B: Factors P^{*i} and Q^{*i}

Following [60, 61], we have

$$P^{*i} = \frac{K_s + \frac{3}{4}\mu_i}{K_i + \frac{3}{4}\mu_i + \pi\alpha\beta_s} \tag{B1}$$

$$Q^{*i} = \frac{1}{5}\left[1 + \frac{8\mu_s}{4\mu_i + \pi\alpha(\mu_s + 2\beta_s)} + 2\frac{K_i + \frac{2}{3}(\mu_i + \mu_s)}{K_i + \frac{4}{3}\mu_i + \pi\alpha\beta_s}\right] \tag{B2}$$

where $\beta_s = \mu_s \frac{(3K_s + \mu_s)}{(3K_s + 4\mu_s)}$.

Appendix C: Wave Propagation Equation of Penny-Shaped Inclusion Model

Following [38], the wave propagation equations based on penny-shaped inclusion are

$$2G\nabla e_{ij} + \lambda_c \nabla e - \alpha_1 M_1 \nabla(\xi^{(1)} - \phi_1\phi_2\varsigma) - \alpha_2 M_2 \nabla(\xi^{(2)} + \phi_1\phi_2\varsigma) = \rho_0 \ddot{u} + \rho_f \ddot{w}_i^{(1)} + \rho_f \ddot{w}_i^{(2)} \tag{C1}$$

$$\alpha_1 M_1 \nabla e - M_1 \nabla(\xi^{(1)} - \phi_1\phi_2\varsigma) = \rho_f \ddot{u} + m_1 \ddot{w}_i^{(1)} + \frac{\eta}{k_1}\frac{\phi_{10}}{\phi_1}\dot{w}^{(1)} \tag{C2}$$

$$\alpha_2 M_2 \nabla e - M_2 \nabla(\xi^{(2)} + \phi_1\phi_2\varsigma) = \rho_f \ddot{u} + m_2 \ddot{w}_i^{(2)} + \frac{\eta}{k_1}\frac{\phi_{10}}{\phi_1}\dot{w}^{(2)} \tag{C3}$$

$$\begin{aligned} &\left(\frac{3}{8} + \frac{\phi_{20}}{2\phi_{10}}\ln\frac{L+R_0}{R_0}\right)\phi_1^2\phi_2\rho_f R_0^2\ddot{\varsigma} \\ &\quad + \left(\frac{3\eta}{8\kappa_2} + \frac{\eta}{2\kappa_1}\ln\frac{L+R_0}{R_0}\right)\phi_{20}\phi_1^2\phi_2 R_0^2\dot{\varsigma} \\ &\quad = \phi_1\phi_2(\alpha_1 M_1 - \alpha_1 M_2)e + \phi_1\phi_2\left(M_2\xi^{(2)} - M_1\xi^{(1)}\right) \\ &\quad + \phi_1^2\phi_2^2(M_1 + M_2)\varsigma \end{aligned} \tag{C4}$$

where $e_{ij} = {}^1\!/_2\left(\delta_j u_i + \delta_i u_j\right)$ are the solid strain components, with $i, j = 1, 2, 3$, $e = \nabla \cdot \mathbf{u}$, $\xi^{(1)} = -\nabla \cdot \mathbf{w}^{(m)}$ is the fluid content increment ($m = 1, 2$ refer to the host and penny-shaped inclusions, respectively), and $\mathbf{w}^{(m)} = \phi_m (\mathbf{U}_m - \mathbf{u})$, where $\mathbf{U} = (U_1, U_2, U_3)^T$ and $\mathbf{u} = (u_1, u_2, u_3)^T$ are the fluid and solid displacements, respectively, and the dot above a variable denotes a partial time derivative. The variation in fluid flow between the host medium and inclusion is denoted by ς. ϕ_{10} and ϕ_{20} are the local porosities of the two skeletons (stiff pores and cracks), $\phi_1 = \phi_{10}v_1$ and $\phi_2 = \phi_{20}v_2$ are the absolute porosities of the two pore types, with v_1 and v_2 their respective volume ratio which satisfy $v_1 + v_2 = 1$, the total porosity is $\phi = \phi_1 + \phi_2$, η is the fluid viscosity, κ_1 and κ_2 are the host and inclusion permeabilities, respectively, ρ_0 and ρ_f are the composite and pore-fluid densities, with $\rho_0 = (1-\phi)\rho_s + \phi\rho_f$ where ρ_s is the grain density, $m_1 = \frac{\tau_1\rho_f}{\phi_1}$ and $m_2 = \frac{\tau_2\rho_f}{\phi_2}$ with $\tau_1 = \frac{1}{2}\left(1 + \frac{1}{\phi_1}\right)$ and $\tau_2 = \frac{1}{2}\left(1 + \frac{1}{\phi_2}\right)$ as the host medium and inclusion tortuosities, respectively. $G = \mu_{\text{SC}}^*$ is the bulk shear modulus of dry rock and the stiffnesses λ_c, α_1, α_2, M_1 and M_2 are given in Appendix D. The characteristic flow length is $L = \left(\frac{R_0^2}{12}\right)^{1/2}$ and R_0 is the inclusion radius.

Appendix D: Stiffness Coefficients

The expressions of the stiffness coefficients are

$$\begin{aligned} \lambda_c &= (1-\phi)K_s - \frac{2}{3}G + \left(2 - \frac{K_s}{K_f}\right)(\phi_1\alpha_1 M_1 + \phi_2\alpha_2 M_2) \\ &\quad - \left(1 - \frac{K_s}{K_f}\right)\left(\phi_1^2 M_1 + \phi_2^2 M_2\right) \end{aligned} \tag{D1}$$

$$\alpha_1 = \frac{\beta\phi_1 K_s}{\gamma K_f} + \phi_1, \quad \alpha_2 = \frac{\beta\phi_2 K_s}{\gamma K_f} + \phi_2 \tag{D2}$$

$$M_1 = \frac{K_f}{\left(\frac{\beta}{\gamma} + 1\right)\phi_1}, \quad M_2 = \frac{K_f}{\left(\frac{1}{\gamma} + 1\right)\phi_2} \tag{D3}$$

$$\gamma = \frac{K_s}{K_f}\left(\frac{\beta\phi_1 + \phi_2}{1 - \phi - \frac{K_b}{K_s}}\right) \tag{D4}$$

$$\beta = \frac{\phi_{20}}{\phi_{10}}\left[\frac{1 - (1 - \phi_{10})\frac{K_s}{K_{b1}}}{1 - (1 - \phi_{20})\frac{K_s}{K_{b2}}}\right] \tag{D5}$$

where $K^*_{SC} = K_b$ is the bulk modulus of the dry rock, $K_i = K_{b1}$ and K_{b2} are the dry-rock moduli of the host medium and inclusions.

Appendix E: Dispersion Equations

Substituting a plane-wave kernel into the differential equations (C1) - (C4), the complex wave number k can be obtained from

$$\begin{vmatrix} a_{11}k^2 + b_{11} & a_{12}k^2 + b_{12} & a_{13}k^2 + b_{13} \\ a_{21}k^2 + b_{21} & a_{22}k^2 + b_{22} & a_{23}k^2 + b_{23} \\ a_{31}k^2 + b_{31} & a_{32}k^2 + b_{32} & a_{33}k^2 + b_{33} \end{vmatrix} = 0, \tag{E1}$$

where

$$\begin{aligned}
&a_{11} = \lambda_c + \tfrac{2}{3}G + \phi_1\phi_2(\alpha_1 M_1 - \alpha_2 M_2)q_1, && b_{11} = -\rho\omega^2 \\
&a_{12} = -\alpha_1 M_1 + \phi_1\phi_2(\alpha_1 M_1 - \alpha_2 M_2)q_2, && b_{12} = \rho_f\omega^2 \\
&a_{13} = -\alpha_2 M_2 + \phi_1\phi_2(\alpha_1 M_1 - \alpha_2 M_2)q_3, && b_{13} = \rho_f\omega^2 \\
&a_{21} = -\alpha_1 M_1 - \phi_1\phi_2 M_1 q_1, && b_{21} = b_{12} \\
&a_{22} = M_1 - \phi_1\phi_2 M_1 q_2, && b_{22} = -M_1\omega^2 + i\omega b_1/\phi_1^2 \\
&a_{23} = -\phi_1\phi_2 M_1 q_3, && b_{23} = 0 \\
&a_{31} = -\alpha_2 M_2 - \phi_1\phi_2 M_2 q_1, && b_{31} = b_{13} \\
&a_{32} = \phi_1\phi_2 M_2 q_2, && b_{32} = 0 \\
&a_{33} = M_2 + \phi_1\phi_2 M_2 q_3,
\end{aligned} \tag{E2}$$

with

$$\begin{aligned}
q_1 &= \phi_1\phi_2(\alpha_1 M_1 - \alpha_2 M_2)/Z \\
q_2 &= -\phi_1\phi_2 M_1/Z \\
q_3 &= -\phi_1\phi_2 M_2/Z \\
Z &= -\omega^2\left(\frac{3}{8} + \frac{\phi_{20}}{2\phi_{10}}\ln\frac{L + R_0}{R_0}\right)\phi_1^2\phi_2\rho_f R_0^2 \\
&\quad + i\omega\left(\frac{3\eta_2}{8\kappa_2} + \frac{\eta_1}{2\kappa_1}\ln\frac{L + R_0}{R_0}\right)\phi_{20}\phi_1^2\phi_2 R_0^2 \\
&\quad - \phi_1^2\phi_1^2(M_1 + M_2)
\end{aligned} \tag{E3}$$

The complex wave velocity is

$$v = \frac{\omega}{k} \tag{E4}$$

where k is the complex P-wavenumber. The P-wave phase velocity is

$$V_p = \left(\mathrm{Re}\left(\frac{1}{v}\right)\right)^{-1} \tag{E5}$$

and the quality factor is

$$Q = \frac{\mathrm{Re}(k^2)}{\mathrm{Im}(k^2)} \tag{E6}$$

with $\omega = 2\pi f$, where f is the frequency [54].

References

1. Zou, C.; Hou, L.; Hu, S.; Zhu, R.; Liu, S.; Yang, Z.; Zhidong, G.; Yang, F.; Yang, C.: Prospect of ultra-deep petroleum onshore China. Energy Explor. Exploit. **32**, 19–40 (2014). https://doi.org/10.1260/0144-5987.32.1.19
2. Lan, X.; Lü, X.; Zhu, Y.; Yu, H.: The geometry and origin of strike-slip faults cutting the Tazhong low rise megaanticline (central uplift, Tarim Basin, China) and their control on hydrocarbon distribution in carbonate reservoirs. J. Nat. Gas Sci. Eng. **22**, 633–645 (2015). https://doi.org/10.1016/j.jngse.2014.12.030
3. Emami Niri, M.; Mehmandoost, F.; Nosrati, H.: Pore-type identification of a heterogeneous carbonate reservoir using rock physics principles: a case study from south-west Iran. Acta Geophys. **1**, 3 (2021). https://doi.org/10.1007/s11600-021-00602-9
4. Mazullo, S.J.; Harris, P.M.: An overview of dissolution porosity development in the deep-burial environment, with examples from carbonate reservoirs in the Permian Basin. Permian Basin Play. Tomorrow's Technol. Today. **91–89**, 125–138 (1991)
5. Pang, X.; Tian, J.; Pang, H.; Xiang, C.; Jiang, Z.; Li, S.: Main progress and problems in research on Ordovician hydrocarbon accumulation in the Tarim Basin. Pet. Sci. **7**, 147–163 (2010). https://doi.org/10.1007/s12182-010-0022-z
6. Esteban, M.; Taberner, C.: Secondary porosity development during late burial in carbonate reservoirs as a result of mixing and/or cooling of brines. J. Geochem. Explor. **78–79**, 355–359 (2003). https://doi.org/10.1016/S0375-6742(03)00111-0
7. Loucks, R.G.; Reed, R.M.; Ruppel, S.C.; Jarvie, D.M.: Morphology, genesis, and distribution of nanometer-scale pores in siliceous mudstones of the mississippian barnett shale. J. Sediment. Res. **79**, 848–861 (2009). https://doi.org/10.2110/jsr.2009.092
8. Chalmers, G.R.; Bustin, R.M.; Power, I.M.: Characterization of gas shale pore systems by porosimetry, pycnometry, surfacearea, and-field emission scanning electron microscopy/transmission electron microscopy image analyses: examples from the Barnett, Woodford, Haynesville, Marcellus, andDoig units. Am. Assoc. Pet. Geol. Bull. **96**, 1099–1119 (2012). https://doi.org/10.1306/10171111052
9. Ba, J.; Ma, R.; Carcione, J.M.; Picotti, S.: Ultrasonic wave attenuation dependence on saturation in tight oil siltstones. J. Pet. Sci. Eng. **179**, 1114–1122 (2019). https://doi.org/10.1016/j.petrol.2019.04.099
10. Ma, R.P.; Ba, J.; Carcione, J.M.; Zhou, X.; Li, F.: Dispersion and attenuation of compressional waves in tight oil reservoirs: Experiments and simulations. Appl. Geophys. **16**, 33–45 (2019). https://doi.org/10.1007/s11770-019-0748-3
11. Smith, T.M.; Sayers, C.M.; Sondergeld, H.C.: Rock properties in low-porosity/low-permeability sandstones. Lead. Edge. **28**, 1–5 (2009)
12. Vernik, L.; Kachanov, M.: Modeling elastic properties of siliciclastic rocks. Geophysics (2010). https://doi.org/10.1190/1.3494031
13. Sakhaee-Pour, A.; Bryant, S.L.: Effect of pore structure on the producibility of tight-gas sandstones. Am. Assoc. Pet. Geol. Bull. **98**, 663–694 (2014). https://doi.org/10.1306/08011312078

14. Sun, Y.; Wu, Q.; Wei, M.; Bai, B.; Ma, Y.: Experimental study of friction reducer flows in microfracture. Fuel **131**, 28–35 (2014). https://doi.org/10.1016/j.fuel.2014.04.050
15. Pimienta, L.; Sarout, J.; Esteban, L.; David, C.; Clennell, M.B.: Pressure-dependent elastic and transport properties of porous and permeable rocks: microstructural control. J. Geophys. Res. Solid Earth. **122**, 8952–8968 (2017). https://doi.org/10.1002/2017JB014464
16. Sarout, J.; Cazes, E.; Delle Piane, C.; Arena, A.; Esteban, L.: Stress-dependent permeability and wave dispersion in tight cracked rocks: Experimental validation of simple effective medium models. J. Geophys. Res. Solid Earth. **122**, 6180–6201 (2017). https://doi.org/10.1002/2017JB014147
17. Brantut, N.; Baker, M.; Hansen, L.N.; Baud, P.: Microstructural control of physical properties during deformation of porous limestone. J. Geophys. Res. Solid Earth. **123**, 4751–4764 (2018). https://doi.org/10.1029/2018JB015636
18. Benaafi, M.; Hariri, M.; Bertotti, G.; Al-Shaibani, A.; Abdullatif, O.; Makkawi, M.: Natural fracture system of the Cambro-Permian Wajid Group, Wadi Al-Dawasir, SW Saudi Arabia. J. Pet. Sci. Eng. **175**, 140–158 (2019). https://doi.org/10.1016/j.petrol.2018.12.022
19. Dvorkin, J.; Alabbad, A.: Velocity-porosity-mineralogy trends in chalk and consolidated carbonate rocks. Geophys. J. Int. **219**, 662–671 (2019). https://doi.org/10.1093/gji/ggz304
20. Zhang, L.; Ba, J.; Fu, L.; Carcione, J.M.; Cao, C.: Estimation of pore microstructure by using the static and dynamic moduli. Int. J. Rock Mech. Min. Sci. **113**, 24–30 (2019). https://doi.org/10.1016/j.ijrmms.2018.11.005
21. Shanley, K.W.; Cluff, R.M.; Robinson, J.W.: Factors controlling prolific gas production from low-permeability sandstone reservoirs: Implications for resource assessment, prospect development, and risk analysis. Am. Assoc. Pet. Geol. Bull. **88**, 1083–1121 (2004). https://doi.org/10.1306/03250403051
22. Byrnes, A.P., Cluff, R.M., Victorine, J., John, W., Stalder, K., Daniel, O., Andrew, K., Owen, M., Troy, H., Joshua, B., Krygowski, D., Whittaker, S.: Analysis of critical permeabilty, capillary pressure and electrical properties for mesaverde tight gas sandstones from western US Basins. (2008). doi:https://doi.org/10.2172/971248
23. Saleh, A.A.; Castagna, J.P.: Revisiting the Wyllie time avarage equation in the case of near-spherical pores. Geophysics **69**, 45–55 (2004). https://doi.org/10.1190/1.1649374
24. Xu, S.; Payne, M.A.: Modeling elastic properties in carbonate rocks. Lead. Edge (Tulsa, OK) **28**, 66–74 (2009). https://doi.org/10.1190/1.3064148
25. Johari, A.; Emami Niri, M.: Rock physics analysis and modelling using well logs and seismic data for characterising a heterogeneous sandstone reservoir in SW of Iran. Explor. Geophys. (2020). https://doi.org/10.1080/08123985.2020.1836956
26. Kumar, M., Han, D.H.: Pore shape effect on elastic properties of carbonate rocks. Soc. Explor. Geophys. 75th SEG Int. Expo. Annu. Meet. SEG 2005. (2005). doi:https://doi.org/10.1190/1.2147969
27. Sayers, C.M.: The elastic properties of carbonates. Lead. Edge (Tulsa, OK) **27**, 1020–1024 (2008). https://doi.org/10.1190/1.2967555
28. Smith, T.; Sondergerld, C.; Ali, O.T.: Microstructural controls on electric and acoustic properties in tight gas sandstones: some emperical data and observations. Lead. Edge. **29**, 1470–1474 (2010). https://doi.org/10.1190/1.3525362
29. Zhao, L.; Nasser, M.; Han, D.H.: Quantitative geophysical pore-type characterization and its geological implication in carbonate reservoirs. Geophys. Prospect. **61**, 827–841 (2013). https://doi.org/10.1111/1365-2478.12043
30. Avseth, P.; Mukerji, T.; Mavko, G.: Quantitative Seismic Interpretation: Applying Rock Physics Tools to Reduce Interpretation Risk. Cambridge University Press, Cambridge (2005)
31. Dvorkin, J.P.; Mavko, G.: Modeling attenuation in reservoir and nonreservoir rock. Lead. Edge (Tulsa, OK) **25**, 194–197 (2006). https://doi.org/10.1190/1.2172312
32. Picotti, S.; Carcione, J.M.; Ba, J.: Rock-physics templates based on seismic. Q. Geophys. (2018). https://doi.org/10.1190/geo2018-0017.1
33. Tucovic, N.; Gegenhuber, N.: Well-log based rock physics template of the Vienna Basin and the underlying Calcereous Alps. Acta Geophys. **65**, 441–451 (2017). https://doi.org/10.1007/s11600-017-0037-6
34. Li, H.; Zhang, J.: Well log and seismic data analysis for complex pore-structure carbonate reservoir using 3D rock physics templates. J. Appl. Geophys. **151**, 175–183 (2018). https://doi.org/10.1016/j.jappgeo.2018.02.017
35. Tan, W.; Ba, J.; Müller, T.; Fang, G.; Zhao, H.: Rock physics model of tight oil siltstone for seismic prediction of brittleness. Geophys. Prospect. **68**, 1554–1574 (2020). https://doi.org/10.1111/1365-2478.12938
36. Pang, M.; Ba, J.; Fu, L.Y.; Carcione, J.M.; Markus, U.I.; Zhang, L.: Estimation of microfracture porosity in deep carbonate reservoirs based on 3D rock-physics templates. Interpretation (2020). https://doi.org/10.1190/INT-2019-0258.1
37. Berryman, G.: Ellipsoidal inclusions Ac "a." J. Acoust. Am. **66**, 1820 (1980)
38. Zhang, L.; Ba, J.; Carcione, J.M.; Sun, W.: Modeling wave propagation in cracked porous media with penny-shaped inclusions. Geophysics (2019). https://doi.org/10.1190/geo2018-0487.1
39. Lu, Z.; Li, Y.; Ye, N.; Zhang, S.; Lu, C.; Li, W.; Cheng, Z.; Ding, X.; Zhu, B.; Huang, B.: Fluid inclusions record hydrocarbon charge history in the Shunbei Area, Tarim Basin. NW China. Geofluids. (2020). https://doi.org/10.1155/2020/8847247
40. Wang, Q.; Hao, F.; Cao, Z.; Tian, J.; Cong, F.: Geochemistry and origin of the ultra-deep Ordovician oils in the Shunbei field, Tarim Basin, China: Implications on alteration and mixing. Mar. Pet. Geol. **123**, 104725 (2021). https://doi.org/10.1016/j.marpetgeo.2020.104725
41. Ni, Z.Y.; Wang, T.G.; Li, M.J.; Chen, Z.H.; Ou, G.X.; Cao, Z.C.: Natural gas characteristics, fluid evolution, and gas charging time of the Ordovician reservoirs in the Shuntuoguole region, Tarim Basin. NW China. Geol. J. **53**, 947–959 (2018). https://doi.org/10.1002/gj.2936
42. Guo, M.Q.; Fu, L.Y.; Ba, J.: Comparison of stress-associated coda attenuation and intrinsic attenuation from ultrasonic measurements. Geophys. J. Int. **178**, 447–456 (2009). https://doi.org/10.1111/j.1365-246X.2009.04159.x
43. David, E.C.; Zimmerman, R.W.: Pore structure model for elastic wave velocities in fluid-saturated sandstones. J. Geophys. Res. Solid Earth. **117**, 1–15 (2012). https://doi.org/10.1029/2012JB009195
44. Mori, T.; Tanaka, K.: Average stress in matrix and average elastic energy of materials with misfitting inclusions. Acta Metall. **21**, 571–574 (1973). https://doi.org/10.1016/0001-6160(73)90064-3
45. Toksoz, M.N.; Johnston, D.H.; Timur, A.: Attenuation of seismic waves in dry and saturated rocks: I. Laboratory measurements. Geophysics. **44**, 681–690 (1979). https://doi.org/10.1190/1.1440970
46. Voigt, W.: Lehrbuch der kristallphysik (mit ausschluss der kristalloptik). B.G. Teubner, Leipzig; Berlin (1910)
47. Reuss, A.: Berechnung der Fließgrenze von Mischkristallen auf Grund der Plastizitätsbedingung für Einkristalle. ZAMM Zeitschrift für Angew. Math. und Mech. 9, 49–58 (1929). doi:https://doi.org/10.1002/zamm.19290090104
48. Hill, R.: The elastic behaviour of a crystalline aggregate. Proc. Phys. Soc. Sect. A. **65**, 349–354 (1952). https://doi.org/10.1088/0370-1298/65/5/307

49. Berryman, J.G.: Long-wavelength propagation in composite elastic media. J. Acoust. Soc. Am. **68**, 1809–1819 (1980). https://doi.org/10.1121/1.385171
50. Batzle, M.; Zhijing, W.: Seismic properties of pore fluids. Geophysics **57**, 1396–1408 (1992). https://doi.org/10.1190/1.1443207
51. Ba, J.; Carcione, J.M.; Nie, J.X.: Biot-Rayleigh theory of wave propagation in double-porosity media. J. Geophys. Res. Solid Earth. **116**, 6202 (2011). https://doi.org/10.1029/2010JB008185
52. Pride, S.R.; Berryman, J.G.; Harris, J.M.: Seismic attenuation due to wave-induced flow. J. Geophys. Res. Solid Earth. (2004). https://doi.org/10.1029/2003jb002639
53. Ba, J.; Xu, W.; Fu, L.-Y.Y.; Carcione, J.M.; Zhang, L.: Rock anelasticity due to patchy saturation and fabric heterogeneity: A double double-porosity model of wave propagation. J. Geophys. Res. Solid Earth. **122**, 1949–1976 (2017). https://doi.org/10.1002/2016JB013882
54. Carcione, J.M.: Wavefields in real media. Theory and numerical simulation of wave propagation in anisotropic, anelastic, porous and electromagnetic media. Elsevier, Hoboken (2014)
55. Ba, J.; Cao, H.; Carcione, J.M.; Tang, G.; Yan, X.F.; Sun, W.T.; Nie, J.X.: Multiscale rock-physics templates for gas detection in carbonate reservoirs. J. Appl. Geophys. **93**, 77–82 (2013). https://doi.org/10.1016/j.jappgeo.2013.03.011
56. Guo, Z.; Li, X.Y.; Liu, C.; Feng, X.; Shen, Y.: A shale rock physics model for analysis of brittleness index, mineralogy and porosity in the Barnett Shale. J. Geophys. Eng. (2013). https://doi.org/10.1088/1742-2132/10/2/025006
57. Klimentos, T.: Attenuation of P- and S-waves as a method of distinguishing gas and condensate from oil and water. Geophysics **60**, 447–458 (1995). https://doi.org/10.1190/1.1889899
58. Li, F.; Zhou, H.; Zhao, T.; Marfurt, K.J.: Unconventional reservoir characterization based on spectrally corrected seismic attenuation estimation. J. Seism. Explor. **25**, 447–461 (2016)
59. Pang, M.; Ba, J.; Carcione, J.M.; Picotti, S.; Zhou, J.; Jiang, R.: Estimation of porosity and fluid saturation in carbonates from rock-physics templates based on seismic Q. Geophys. **84**, M25–M36 (2019). https://doi.org/10.1190/geo2019-0031.1
60. Berryman, J.G.: Mixture theories for rock properties. In: Ahrens, T.J. (Ed.) Rock physics and phase relations: a handbook of physical constants, pp. 205–228. American Geophysical Union (AGU), Washington, DC (1995)
61. Mavko, G.; Mukerji, T.; Dvorkin, J.: The rock physics handbook. Cambridge University Press, Cambridge (2009)